Progress In Electromagnetics Research, Vol. 177, 127–137, 2023

Two-Dimensional Acoustic Asymmetric Vortex Focusing Lens by Binary-Phase Mode Converters

Yin Wang[1], Hong-Yu Zou[1], Yu-Jing Lu[1], Shuai Gu[1], Jiao Qian[1], Jian-Ping Xia[1], Yong Ge[1], Hong-Xiang Sun[1, 2, *], Shou-Qi Yuan[1], and Xiao-Jun Liu[2, 3, *]

Abstract—Recently, the study of acoustic vortex beams has attracted a great attention owing to its potential applications in medical ultrasound imaging and trapping particles. In some special applications of medical ultrasound, it needs the simultaneous realization of vortex focusing and asymmetric transmission in three-dimensional (3D) space. However, the design of a two-dimensional (2D) device with acoustic asymmetric vortex focusing (AAVF) remains a challenge. To overcome it, we experimentally demonstrate a 2D AAVF lens composed of three types of binary-phase mode converters. By simultaneously introducing the phase profiles of acoustic focusing and vortex caused by the mode converters, we design a 2D AAVF lens with the topological charge $n = 2$, i.e., the sound energy can pass through the lens from the upper side and forms a vortex focus in 3D space; however, it cannot transmit through the lens from the other side. The vortex focusing and asymmetric transmission arise from the phase manipulation and the conversion between the zero-order and first-order waves caused by the mode converters, respectively. The measured fractional bandwidth can reach about 0.19. The proposed lens has the advantages of high-performance AAVF, broad bandwidth, and complex sound modulation in 3D space, which provides diverse routes for designing 3D multi-functional sound devices with promising applications in medical ultrasound.

1. INTRODUCTION

In the past few years, the study on acoustic vortex beams has become a hot topic due to its potential applications in a variety of important fields, such as acoustic communications [1, 2], levitation of organisms [3, 4], and medical ultrasound [5, 6]. Acoustic vortex beam has a typical characteristic of orbital angular momentum, which also provides a new degree of freedom for sound manipulations in sub-diffraction imaging [7, 8], and micro-particle absorption and rotations [9–12]. Traditionally, by designing an active phased array [13–15] with the conversion between acoustic and electronic signals, the manipulation of underwater micro-particles by vortex beams was realized experimentally. The active design has a relative high efficiency; however, complex experimental equipment and high cost seriously limit its practical applications.

To overcome these problems, acoustic metamaterials [16–22] and metasurfaces [23–29] were introduced to design passive acoustic lenses with integer [30, 31] and fractional [32, 33] vortex beams, which have the advantages of low cost and subwavelength structure. Based on rotational phase profiles caused by structural design, such as thickness-gradient structures [34, 35], spiral arms [36, 37], and Helmholtz resonators [38, 39], the acoustic vortex beams can be observed around structure surfaces or

Received 25 April 2023, Accepted 8 July 2023, Scheduled 28 July 2023

* Corresponding author: Hong-Xiang Sun (jsdxshx@ujs.edu.cn), Xiao-Jun Liu (liuxiaojun@nju.edu.cn).

[1] Research Center of Fluid Machinery Engineering and Technology, School of Physics and Electrical Engineering, School of Computer Science and Communication Engineering, Jiangsu University, Zhenjiang 212013, China. [2] State Key Laboratory of Acoustics, Institute of Acoustics, Chinese Academy of Sciences, Beijing 100190, China. [3] Key Laboratory of Modern Acoustics, Department of Physics and Collaborative Innovation Center of Advanced Microstructures, Nanjing University, Nanjing 210093, China.

in external waveguides with a hard boundary. In addition, based on an artificial structure with discrete Archimedean spiral slits, the effect of acoustic vortex focusing can be realized in three-dimensional (3D) free space [40–43], which effectively avoids the diffusion of the vortex. Despite the fact that a variety of high-performance vortex lenses were designed successively, the realization of vortex beams with other exotic effects, such as asymmetric acoustic vortex focusing (AAVF), was seldom reported. The AAVF has a great potential in medical ultrasound [44, 45], in which the vortex beams with focusing effect can be used to capture or remove cells, and their associated reflected energy is prohibited to return to devices, improving the service life of acoustic transducers greatly. Based on the extended generalized Snell's law, a type of asymmetric acoustic vortex caused by dual-layer gradient-phase metasurfaces was observed in a waveguide structure [46, 47]. However, the dual-layer systems inevitably increase the difficulty in their practical application, and meanwhile the vortex beam requires the waveguide to support its propagation. The design of a two-dimensional (2D) monolayer acoustic lens with AAVF in 3D space still faces great challenges.

In this work, we propose a broadband 2D AAVF lens based on three types of binary-phase mode converters composed of two pairs of out-of-phase unit cells and a step waveguide [48]. Based on the phase profiles of acoustic focusing and vortex caused by 48 mode converters, we experimentally design a type of 2D AAVF lens with $n = 2$, in which the vortex focusing and asymmetric transmission are attributed to the phase manipulation and the conversion between the zero-order and first-order waves caused by the mode converters, respectively. Moreover, we experimentally measured the working bandwidth of the AAVF lens, and the fractional bandwidth can reach about 0.19. The measured results agree well with the simulated ones.

2. RESULTS AND DISCUSSIONS

Figure 1 schematically shows asymmetric vortex focusing caused by a 2D AAVF lens, in which the abbreviations TI and BI represent the normal incidence of acoustic plane waves from the top and bottom sides of the lens, respectively. We can see that the acoustic wave can transmit through the lens, and forms a vortex focus on the bottom side for TI; however, the acoustic wave cannot transmit through the lens for BI, showing a typical characteristic of AAVF. To theoretically design it, we introduce the

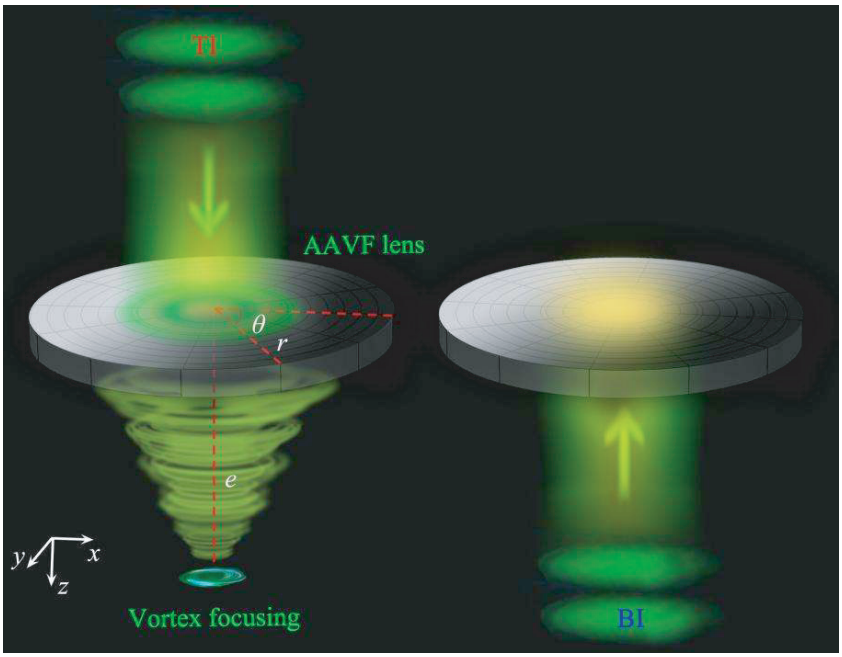

Figure 1. Schematic of asymmetric vortex focusing caused by the 2D AAVF lens for TI and BI.

phase profile of a vortex beam in free space as follows

$$\varphi(\theta) = n\theta, \tag{1}$$

where n is the topological charge of the vortex beam [40], and θ is the azimuth angle. Here, by introducing acoustic vortex focusing the phase profile of the AAVF lens in the x-y plane based on the generalized Snell's law [49] can be written as

$$\varphi = -k\sqrt{r^2 + e^2} + n\theta, \tag{2}$$

where $k = 2\pi f/c$ is the wave number in air, and c and f represent the sound velocity and the frequency, respectively. Parameters $r = \sqrt{x^2 + y^2}$ and e are the radial length and the focal length of the lens, respectively, and the azimuth angle θ satisfies $\tan\theta = x/y$. Based on Eq. (2), we can realize the effect of acoustic vortex focusing.

Figure 2(a) shows the photograph of the designed 2D AAVF lens (with a radius $r = 25.8\,\text{cm}$) composed of a central solid cylinder and twelve fan-shaped structures (red shaded region), in which each fan-shaped structure (shown in the upper inset) is constructed by four binary-phase mode converters. The 2D AAVF lens is made of epoxy resin to satisfy the condition of the hard sound boundary. As shown in Figure 2(b), the binary-phase mode converter consists of two pairs of out-of-phase unit cells (denoted as A and B) and a step waveguide on the upper side. Both unit cells (with a length l =4 cm and a width $w = 1.2\,\text{cm}$) are composed of eight Helmholtz resonators on both sides and a central channel. To design the out-of-phase unit cells, we adjust the volume of each Helmholtz resonator by changing the width w_1 of the central channel, and therefore different resonant frequencies and phase delays of sound can be realized. Based on two pairs of out-of-phase unit cells, we can realize the conversion between the zero-order and first-order waves (see the Supplementary Material). It is noted that the zero-order wave can pass through the waveguide with an arbitrary width, while the first-order wave can only transmit through the waveguide with the width larger than a half wavelength. Here, the selected width w_4 of the step waveguide is smaller than a half wavelength of sound, which can be used to prohibit the propagation of the first-order wave realizing asymmetric sound transmission. Throughout this work, we use the numerical software of COMSOL Multiphysics to simulate the performance of AAVF. The structure parameters of the mode converter are selected as $w_2 = 1.3\,\text{cm}$, $w_3 = 4.8\,\text{cm}$, $w_4 = 2\,\text{cm}$, l_1 =0.9 cm, l_2 =0.15 cm, $l_3 = 1.5\,\text{cm}$, and $d = 0.08\,\text{cm}$, and the acoustic wavelength λ is selected as 5 cm (viz., the frequency $f = 6860\,\text{Hz}$ in air). The material parameters of air are $\rho = 1.21\,\text{kg/m}^3$ and $c = 343\,\text{m/s}$ in the simulations.

To design out-of-phase unit cells, we simulate the transmission and phase delay spectra through a single phased unit cell with different values of w_1, which are shown in Figure 2(c). Here, we select six phased unit cells (color dots) with an equally spaced phase delay from 0 to 2π, and their transmission coefficients are larger than 0.9. Thus, based on the six phased unit cells, we design three types of binary-phase mode converters, denoted as I, II, and III, which are shown in Figure 2(d). To present their characteristics, we simulate the pressure distributions caused by the mode converters under the excitation of the zero-order wave for TI and BI, and the corresponding results are shown in Figures 2(e) and 2(f), respectively. We can see that, for TI, the zero-order wave can transmit through the step waveguide and phased unit cells and reach the bottom side of the mode converter as the form of the converted first-order wave. However, for BI, the zero-order wave is converted into the first-order wave by the phased unit cells, but cannot pass through the step waveguide, which arises from the fact that the opening width of the step waveguide is smaller than a half wavelength of sound. Beyond that, we simulate the transmittance spectra of the mode converters I, II, and III for TI and BI (see the Supplementary Material). The simulated results present the typical characteristic of asymmetric transmission of sound for each mode converter.

By using the three binary-phase mode converters, we here design a broadband 2D AAVF lens with $e = 20\,\text{cm}$ and $n = 2$. Based on Eq. (2), we theoretically calculate the continuous phase profile of the lens in the x-y plane [Figure 3(a)], which exhibits a typical characteristic of the vortex beam with $n = 2$. Based on the theoretical phase profile, we use 48 mode converters to design the AAVF lens. However, there inevitably exist gaps with the size smaller than that of the mode converters, and thus we use epoxy resin [shown as light gray solid in Figure 3(b)] to fill the gaps to connect the adjacent mode converters. As shown in Figure 3(b), the phase profile of the AAVF lens is consistent with that

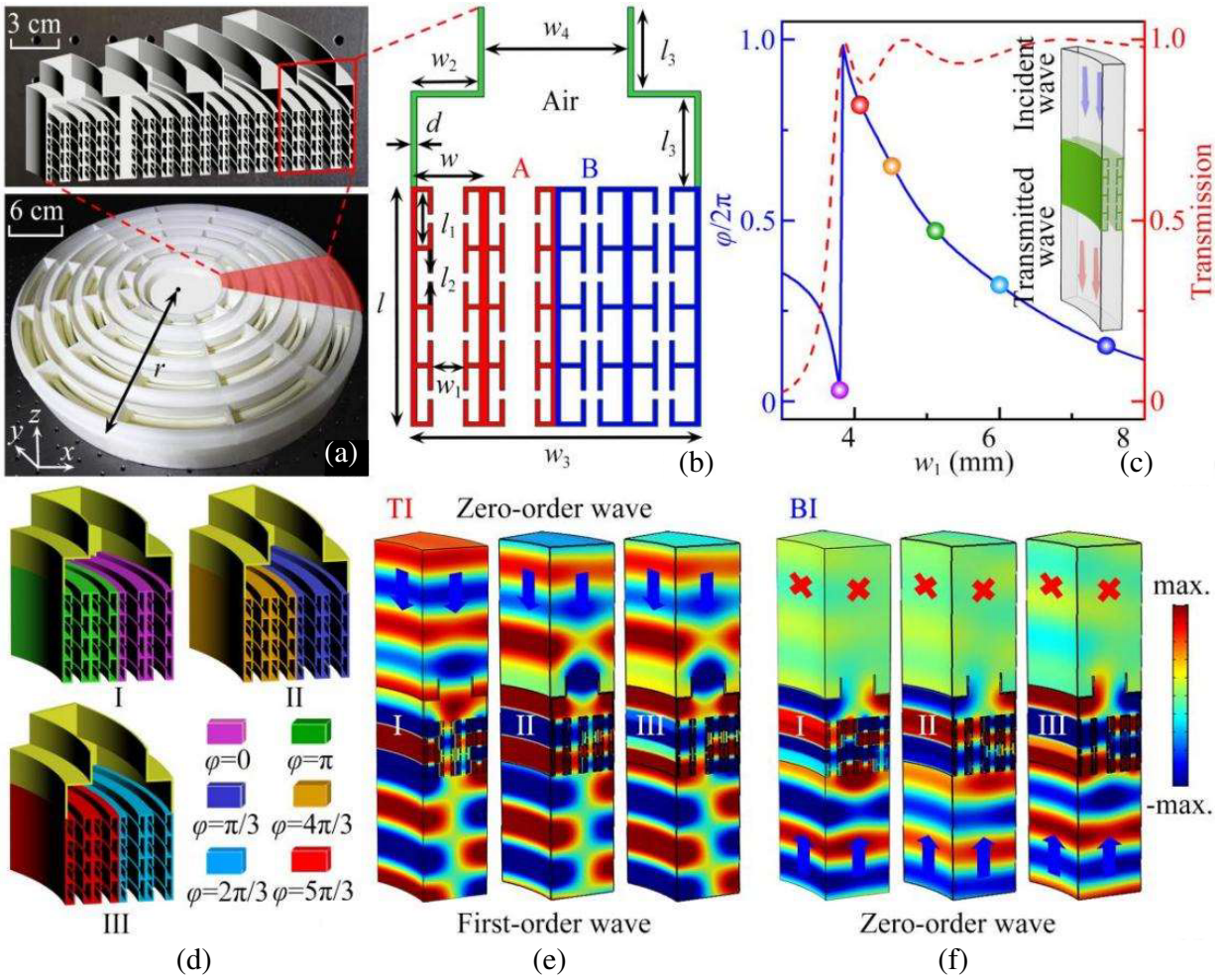

Figure 2. (a) Photograph of the 2D AAVF lens composed of a central solid cylinder and twelve fan-shaped structures with four binary-phase mode converters. (b) Schematic of a mode converter composed of two pairs of out-of-phase unit cells (A and B) and a step waveguide on the upper side. (c) Simulated phase delay (blue solid line) and transmission spectra (red dashed line) as a function of the parameter w_1 at 6860 Hz. The phase delays caused by the selected six phased unit cells (color dots) from the left to the right are 0, $5\pi/3$, $4\pi/3$, π, $2\pi/3$, $\pi/3$, and the corresponding values of w_1 are 0.384, 0.406, 0.45, 0.51, 0.6 and 0.75 cm, respectively. (d) Schematic of three types of binary-phase mode converters I, II, and III constructed by the selected six phased unit cells in (c). Simulated pressure distributions caused by the mode converters I, II, and III for (e) TI and (f) BI at 6860 Hz, respectively.

in Figure 3(a). Therefore, we can realize the AAVF lens based on the theoretically calculated phase profile, and the transmitted vortex focusing can be realized based on the phase modulation.

Figures 4(a) and 4(b) show the simulated intensity distributions ($|p|^2$) through the 2D AAVF lens for TI and BI, respectively. As shown in Figure 4(a), we can see that the sound energy can pass through the lens and is focused as the shape of a narrow hollow cylinder for TI, in which the energy at the central region is almost zero, showing typical characteristics of both acoustic focusing and vortex. However, the sound energy cannot transmit through the lens for BI [shown in Figure 4(b)], showing a typical characteristic of AAVF. This is because the converted first-order wave cannot pass through the step waveguide of each mode converter. Furthermore, we simulate the intensity distributions created by the lens composed of the binary-phase mode converters without the step waveguide. The results show that the effect of vortex focusing exists for both TI and BI (see the Supplemental Material), further demonstrating that the asymmetric sound transmission is determined by the step waveguide.

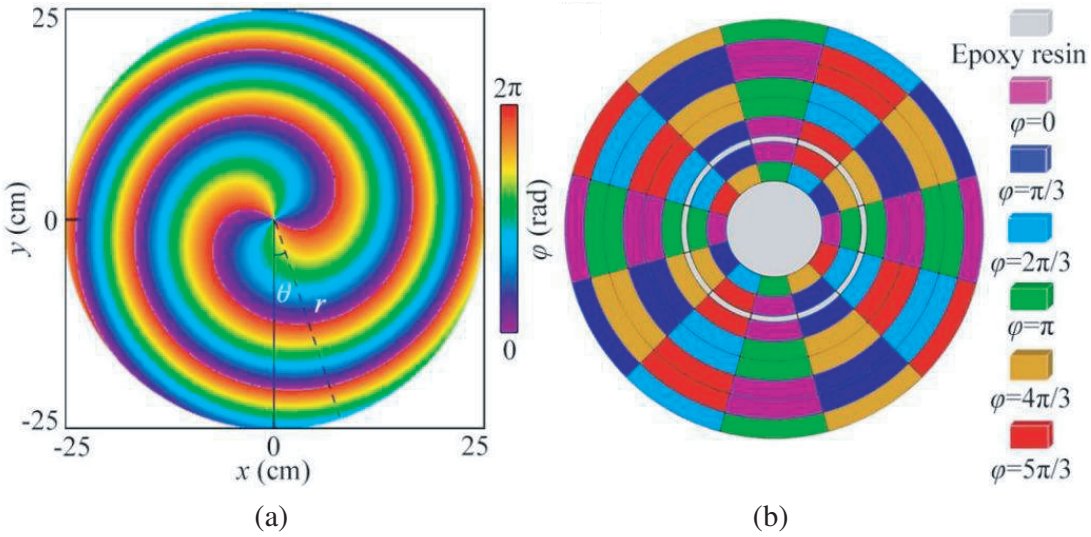

Figure 3. (a) Theoretical continuous phase delay of the 2D AAVF lens in the xy plane at 6860 Hz. (b) Designed 2D AAVF lens composed of 48 binary-phase mode converters.

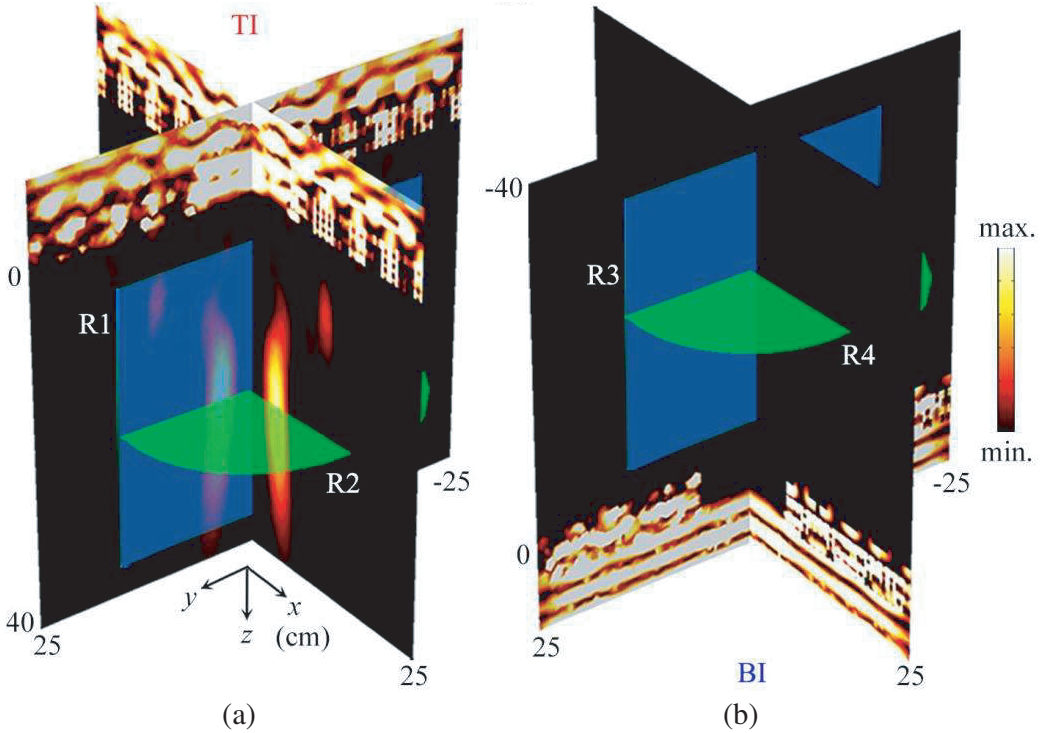

Figure 4. Simulated intensity distributions caused by the AAVF lens for (a) TI and (b) BI at 6860 Hz.

To demonstrate the AAVF performance of the lens, we conduct an experiment to measure the intensity and phase distributions caused by the lens in R1 and R2 for TI, and R3 and R4 for BI of Figure 4. Figure 5(a) schematically shows the experimental setup, in which the sample of the AAVF lens is placed in 3D free space. The incident plane wave is generated from a loudspeaker driven by a power amplifier, and the distance between the loudspeaker and sample is 1 m. Additionally, we use two 0.25-in-diameter microphones to measure the pressure amplitude and phase distributions in the

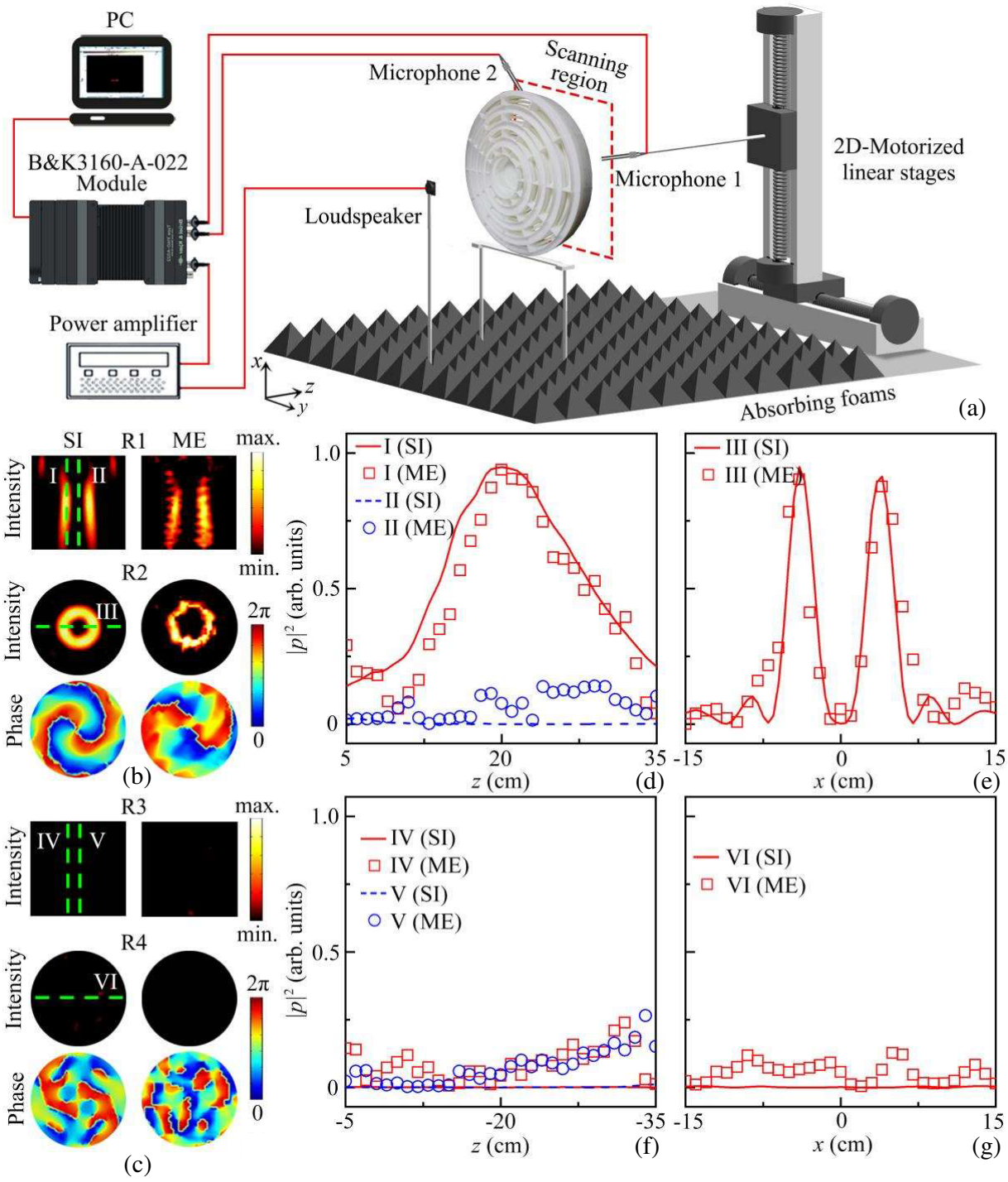

Figure 5. (a) Experimental set-up. Simulated (SI) and measured (ME) intensity and phase distributions caused by the AAVF lens at 6860 Hz in (b) R1 (the x-z plane at $y = 0$) and R2 (the x-y plane at $z = 20$ cm) for TI, and (c) R3 (the x-z plane at $y = 0$) and R4 (the x-y plane at $z = -20$ cm) for BI. Measured and simulated intensity profiles along the (d) lines I, II, and (e) III in (b) and along the (f) lines IV V, and (g) VI in (c).

scanning region, in which microphone 1 is adopted to detect sound signals in the scanning regions moved by two-dimensional motorized linear stages, and microphone 2 is used as a reference. As shown in Figure 5(b), we can see that the sound energy is focused as two focal regions in R1 and a ring-shaped

region in R2. The phase distribution in R2 presents a typical characteristic of a vortex beam with $n = 2$ for TI. The measured results agree well with the simulated ones. Additionally, in R3 and R4 of Figure 5(c), we observe that no sound energy can pass through the lens, and the vortex characteristic does not exist, further experimentally verifying the performance of the 2D AAVF lens.

Figures 5(d)–5(g) show the measured intensity profiles along the lines I-VI in Figures 5(b) and 5(c), and the simulated results are also presented for comparison. As shown in Figure 5(d), it is observed that the focus is located at $z = 20$ cm in line I, and the intensities along line I are much larger than those along line II for TI owing to the existence of the phase singularity along line II. Moreover, as shown in Figure 5(e), two acoustic energy peaks exist on both sides of $x = 0$ along line III, and the intensity at $x = 0$ is close to zero, showing a typical characteristic of vortex focusing. For the case of BI [Figures 5(f) and 5(g)], the intensities along lines IV-VI are close to zero, indicating that the sound energy cannot pass through the lens. The measured intensity distributions agree with the simulated ones, which experimentally demonstrates the performances of the lens. In addition to the lens with $n = 2$, we design the 2D AAVF lenses with $n = 1$ and 3, and the simulated results are presented in the Supplementary Material.

Finally, we experimentally demonstrate the bandwidth of the 2D AAVF lens. Figures 6(a)–6(d) show the simulated intensity distributions created by the 2D AAVF lens for TI and BI at four selected

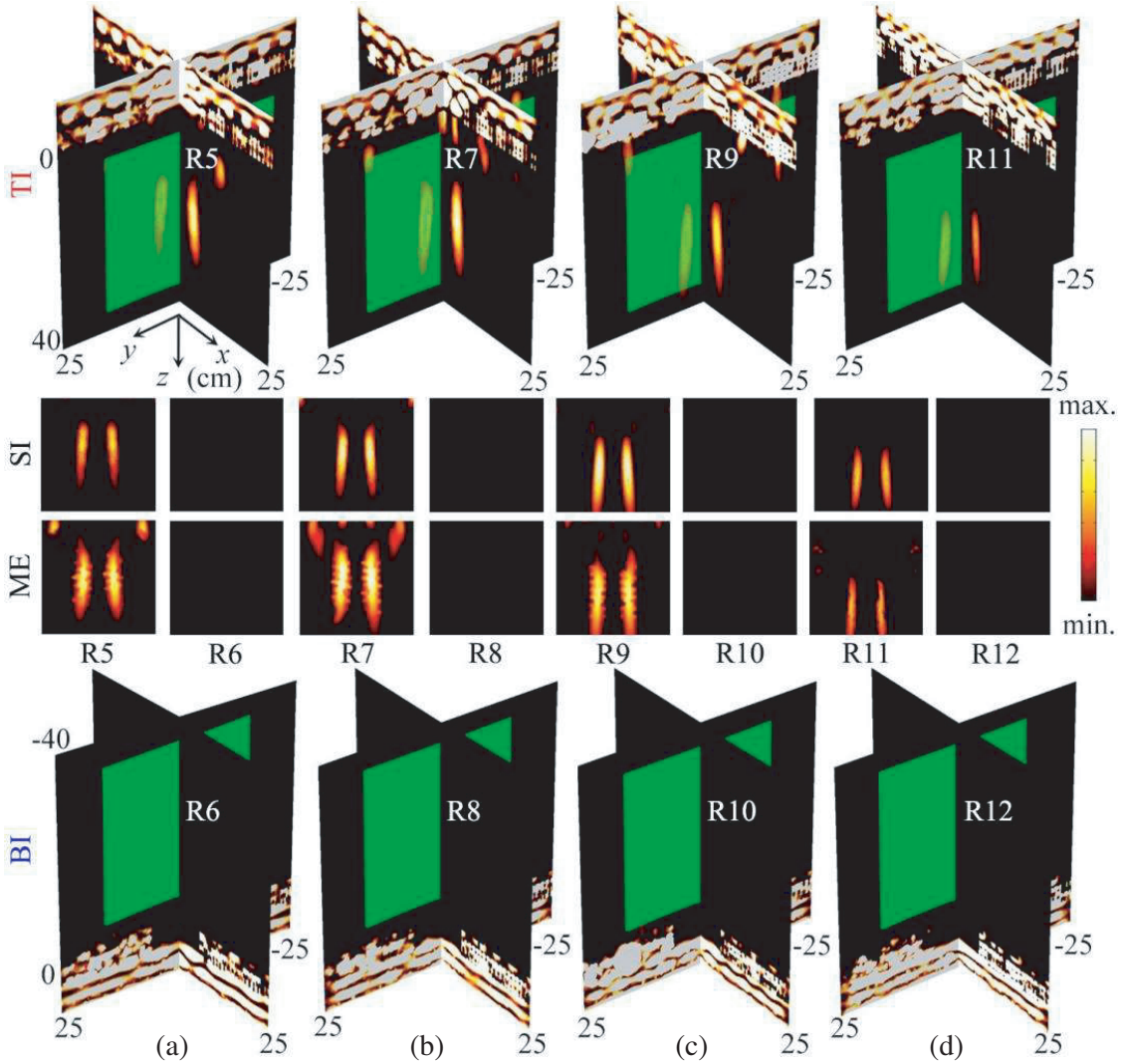

Figure 6. Measured and simulated intensity distributions caused by the 2D AAVF lens for TI and BI at (a) 6.2, (b) 6.6, (c) 7.0 and (d) 7.4 kHz.

frequencies. We can observe that, with the increase of frequency, the focal length gradually increases for TI, and the characteristics of the focus are the same as those in Figure 4(a). Beyond that, the acoustic wave cannot pass through the lens for BI. The measured and simulated results in R5–R12 at these frequencies are presented in the middle region, in which the measured results agree well with the simulated ones. The measured results demonstrate that the bandwidth of the 2D AAVF lens can exceed 1.2 kHz, and the fractional bandwidth is larger than 0.19, showing a broadband characteristic of the lens. Moreover, we simulate the contrast ratio R_c of the AAVF lens, which is shown in the Supplementary Material. The simulated contrast ratios are larger than 0.8 in the range 6.2–7.4 kHz, indicating high-performance AAVF of the designed lens.

3. CONCLUSIONS

In conclusion, we have demonstrated a broadband 2D AAVF lens based on three types of binary-phase mode converters. The results show that the mode converters are composed of two pairs of out-of-phase unit cells and a step waveguide, and can achieve the mode conversion between the zero-order and first-order waves and asymmetric acoustic propagation in 3D space, which arises from the phase manipulation and the narrow opening width of the step waveguide, respectively. Based on 48 mode converters, we experimentally design a broadband 2D AAVF lens with the topological charge $n = 2$, and the fractional bandwidth of AAVF can reach about 0.19. In the working band of AAVF, the sound energy can transmit through the lens for TI and forms a vortex focus in 3D space. However, the acoustic wave cannot transmit through the lens for BI. This is because the converted first-order wave cannot pass through the step waveguide of the mode converters. Finally, by adjusting the phase profiles of the lens, we numerically design the 2D AAVF lenses with $n = 1$ and 3. Our work provides diverse routes for designing 2D multifunctional acoustic devices of vortex beams and has a potential application for non-contact manipulation for trapping particles and medical ultrasound imaging.

SUPPORTING INFORMATION

This part provides the description of the theory of conversion between zero-order and first-order waves, the transmittance spectra of mode converters I, II, and III, the symmetric acoustic vortex focusing caused by 2D AAVF lens without step waveguides, the simulated intensity and phase distributions caused by 2D AAVF lens with $n = 1$ and 3, and the contrast ratio of AAVF lens.

ACKNOWLEDGMENT

Y. W. and H.-Y. Z. contributed equally to this work. This work was supported by the National Natural Science Foundation of China (Grant Nos. 12274183, 12174159, and 11834008), the National Key R&D Program of China (Grant No. 2020YFC1512403), and the Postgraduate Research and Practice Innovation Program of Jiangsu Province (Grant No. KYCX20_3072).

REFERENCES

1. Shi, C. Z., M. Dubois, Y. Wang, and X. Zhang, "High-speed acoustic communication by multiplexing orbital angular momentum," *Proc. Natl. Acad. Sci. U. S. A.*, Vol. 114, No. 28, 7250–7253, 2017.
2. Li, X. J., Y. Z. Li, Q. Y. Ma, G. P. Guo, J. Tu, and D. Zhang, "Principle and performance of orbital angular momentum communication of acoustic vortex beams based on single-ring transceiver arrays," *J. Appl. Phys.*, Vol. 127, No. 12, 124902, 2020.
3. Jiménez-Gambín, S., N. Jiménez, and F. Camarena, "Transcranial focusing of ultrasonic vortices by acoustic holograms," *Phys. Re. Applied*, Vol. 14, No. 15, 054070, 2020.
4. Cao, J. M., K. X. Yang, X. S. Fang, L. Guo, Y. Li, and Q. Cheng, "Holographic tomography of dynamic three-dimensional acoustic vortex beam in liquid," *Appl. Phys. Lett.*, Vol. 119, No. 14, 143501, 2021.

5. Melde, K., E. Choi, Z. Wu, S. Palagi, T. Qiu, and P. Fischer, "Acoustic fabrication via the assembly and fusion of particles," *Adv. Mater.*, Vol. 30, No. 3, 1704507, 2018.
6. Lim, M. X., A. Souslov, V. Vitelli, and H. M. Jaeger, "Cluster formation by acoustic forces and active fluctuations in levitated granular matter," *Nat. Phys.*, Vol. 15, No. 5, 460–464, 2019.
7. Meng, L., F. Cai, F. Li, W. Zhou, L. Niu, and H. Zheng, "Acoustic tweezers," *J. Phys. D: Appl. Phys.*, Vol. 52, No. 27, 273001, 2019.
8. Wu, P. Y., Z. Ya, Y. Li, M. T. Zhu, L. Zhang, Y. J. Zong, S. F. Guo, and M. X. Wan, "Focused acoustic vortex-regulated composite nanodroplets combined with checkpoint blockade for high-performance tumor synergistic therapy," *ACS Appl. Mater. Inter.*, Vol. 14, No. 27, 30466, 2022.
9. Zhang, L. K., "Reversals of orbital angular momentum transfer and radiation torque," *Phys. Rev. Applied*, Vol. 10, No. 3, 034039, 2018.
10. Li, Y. Z., G. P. Guo, J Tu, Q. Y. Ma, X. S. Guo, D. Zhang, and O. A. Sapozhnikov, "Acoustic radiation torque of an acoustic-vortex spanner exerted on axisymmetric objects," *Appl. Phys. Lett.*, Vol. 112, No. 25, 254101, 2018.
11. Baresch, D., J. L. Thomas, and R. Marchiano, "Orbital angular momentum transfer to stably trapped elastic particles in acoustical vortex beams," *Phys. Rev. Lett.*, Vol. 121, No. 7, 074301, 2018.
12. Li, J. F., A. Crivoi, X. Y. Peng, L. Shen, Y. J. Pu, Z. Fan, and S. A. Cummer, "Three dimensional acoustic tweezers with vortex streaming," *Commun. Phys.*, Vol. 4, No. 1, 113, 2021.
13. Riaud, A., J. L. Thomas, E. Charron, A. Bussonnière, O. B. Matar, and M. Baudoin, "Anisotropic swirling surface acoustic waves from inverse filtering for on-chip generation of acoustic vortices," *Phys. Rev. Applied*, Vol. 4, No. 3, 034004, 2015.
14. Muelas-Hurtado, R. D., J. L. Ealo, and K. Volke-Sepúlveda, "Active-spiral Fresnel zone plate with tunable focal length for airborne generation of focused acoustic vortices," *Appl. Phys. Lett.*, Vol. 116, No. 11, 114101, 2020.
15. Huang, H. F. and H. M. Huang, "Millimeter-wave wideband high effeciency circular airy OAM multibeams with multiplexing OAM modes based on transmission metasurfaces," *Progress In Electromagnetics Research*, Vol. 173, 151–159, 2022.
16. Liang, Z. and J. Li, "Extreme acoustic metamaterial by coiling up space," *Phys. Rev. Lett.*, Vol. 108, No. 11, 114301, 2012.
17. Cummer, S. A., J. Christensen, and A. Alù, "Controlling sound with acoustic metamaterials," *Nat. Rev. Mater.*, Vol. 1, No. 3, 16001, 2016.
18. Wu, Y., M. Yang, and P. Sheng, "Perspective: Acoustic metamaterials in transition," *J. Appl. Phys.*, Vol. 123, No. 9, 090901, 2018.
19. Fan, X. D., Z. Zou, and L. Zhang, "Acoustic vortices in inhomogeneous media," *Phys. Rev. Res.*, Vol. 1, No. 3, 032014, 2019.
20. Ma, F., J. Chen, and J. H. Wu, "Experimental study on performance of time reversal focusing," *J. Phys. D: Appl. Phys.*, Vol. 53, No. 5, 055302, 2019.
21. Jia, D., Y. Wang, Y. Ge, S. Q. Yuan, and H. X. Sun, "Tunable topological refractions in valley sonic crystals with triple valley hall phase transitions," *Progress In Electromagnetics Research*, Vol. 172, 13–22, 2021.
22. Wang, B. B., Y. Ge, S. Q. Yuan, D. Jia, and H. X. Sun, "Exceptional ring by non-hermitian sonic crystals," *Progress in Electromagnetics Research*, Vol. 176, 1–10, 2023.
23. Ye, L. P., C. Y. Qiu, J. Lu, K. Tang, H. Jia, M. Ke, S. Peng, and Z. Y. Liu, "Making sound vortices by metasurfaces," *AIP Adv.*, Vol. 6, No. 8, 085007, 2016.
24. Li, J., A. Díaz-Rubio, C. Shen, Z. Jia, S. Tretyakov, and S. A. Cummer, "Highly efficient generation of angular momentum with cylindrical bianisotropic metasurfaces," *Phys. Rev. Applied*, Vol. 11, No. 2, 024016, 2019.
25. Jiang, X., D. A. Ta, and W. Q. Wang, "Modulation of orbital-angular-momentum symmetry of nondiffractive acoustic vortex beams and realization using a metasurface," *Phys. Rev. Applied*, Vol. 14, No. 3, 034014, 2020.

26. Zhang, H. K., W. X. Zhang, Y. H. Liao, X. M. Zhou, J. F. Li, G. K. Hu, and X. D. Zhang, "Creation of acoustic vortex knots," *Nat. Commun.*, Vol. 11, No. 1, 3956, 2020.
27. Fan, S. W., Y. F. Wang, L. Y. Cao, Y. F. Zhu, A. L. Chen, B. Vincent, B. Assouar, and Y. S. Wang, "Acoustic vortices with high-order orbital angular momentum by a continuously tunable metasurface," *Appl. Phys. Lett.*, Vol. 116, No. 16, 163504, 2020.
28. Jiménez, N., J. P. Groby, and V. Romero-García, "Spiral sound-diffusing metasurfaces based on holographic vortices," *Sci. Rep.*, Vol. 11, No. 1, 1–13, 2021.
29. Han, T. C., K. H. Wen, Z. X. Xie, and X. L. Yue, "An ultra-thin wideband reflection reduction metasurface based on polarization conversion," *Progress In Electromagnetics Research*, Vol. 173, 1–8, 2022.
30. Long, Y., D. M. Zhang, C. W. Yang, J. M. Ge, H. Chen, and J. Ren, "Realization of acoustic spin transport in metasurface waveguides," *Nat. Commun.*, Vol. 11, No. 1, 4716, 2020.
31. Gong, K. M., X. Zhou, and J. L. Mo, "Continuously tuneable acoustic metasurface for high order transmitted acoustic vortices," *Smart Mater. Struct.*, Vol. 31, No. 11, 115001, 2022.
32. Hong, Z. Y., J. Zhang, and B. W. Drinkwater, "On the radiation force fields of fractional-order acoustic vortices," *EPL*, Vol. 110, No. 1, 14002, 2015.
33. Jia, Y. R., Q. Wei, D. J. Wu, Z. Xu, and X. J. Liu, "Generation of fractional acoustic vortex with a discrete Archimedean spiral structure plate," *Appl. Phys. Lett.*, Vol. 112, No. 17, 173501, 2018.
34. Ealo, J. L., J. C. Prieto, and F. Seco, "Airborne ultrasonic vortex generation using flexible ferroelectrets," *IEEE Trans. Ultrason. Ferroelectr. Freq. Control*, Vol. 58, No. 8, 1651–1657, 2011.
35. Wunenburger, R., J. I. V. Lozano, and E. Brasselet, "Acoustic orbital angular momentum transfer to matter by chiral scattering," *New J. Phys.*, Vol. 17, No. 1, 103022, 2015.
36. Jiang, X., J. J. Zhao, S. L. Liu, B. Liang, X. Y. Zou, J. Yang, C. W. Qiu, and J. C. Cheng, "Broadband and stable acoustic vortex emitter with multi-arm coiling slits," *Appl. Phys. Lett.*, Vol. 108, No. 20, 203501, 2016.
37. Jiménez, N., V. Romero-García, L. M. García-Raffi, F. Camarena, and K. Staliunas, "Sharp acoustic vortex focusing by Fresnel-spiral zone plates," *Appl. Phys. Lett.*, Vol. 112, No. 20, 204101, 2018.
38. Jiang, X., Y. Li, B. Liang, J. C. Cheng, and L. Zhang, "Convert acoustic resonances to orbital angular momentum," *Phys. Rev. Lett.*, Vol. 117, No. 3, 034301, 2016.
39. Guo, Z. Y., H. J. Liu, H. Zhou, K. Y. Zhou, S. M. Wang, F. Shen, Y. B. Gong, J. Gao, S. T. Liu, and K. Guo, "High-order acoustic vortex field generation based on a metasurface," *Phys. Rev. E*, Vol. 100, No. 5, 053315, 2019.
40. Chen, D. C., Q. X. Zhou, X. F. Zhu, Z. Xu, and D. J. Wu, "Focused acoustic vortex by an artificial structure with two sets of discrete Archimedean spiral slits," *Appl. Phys. Lett.*, Vol. 115, No. 8, 083501, 2019.
41. Guo, S. F., X. Y. Guo, X. Wang, X. Du, P. Y. Wu, A. Bouakaz, and M. X. Wan, "Manipulation of nanodroplets via a nonuniform focused acoustic vortex," *Phys. Rev. Applied*, Vol. 13, No. 3, 034009, 2020.
42. Li, X. R., Y. R. Jia, Y. C. Luo, J. Yao, and D. J. Wu, "Mixed focused-acoustic-vortices generated by an artificial structure plate engraved with discrete rectangular holes," *Appl. Phys. Lett.*, Vol. 118, No. 4, 043503, 2021.
43. Li, X. R., D. J. Wu, Y. C. Luo, J. Yao, and X. J. Liu, "Coupled focused acoustic vortices generated by degenerated artificial plates for acoustic coded communication," *Adv. Mater. Techonl.*, Vol. 7, No. 9, 2200102, 2022.
44. Baudoin, M., J. C. Gerbedoen, A. Riaud, O. B. Matar, N. Smagin, and J. L. Thomas, "Folding a focalized acoustical vortex on a flat holographic transducer: Miniaturized selective acoustical tweezers," *Sci. Adv.*, Vol. 5, No. 4, eaav1967, 2019.
45. Baudoin, M., J. L. Thomas, R. A. Sahely, J. C. Gerbedoen, Z. Gong, A. Sivery, O. B. Matar, N. Smagin, P. Favreau, and A. Vlandas, "Spatially selective manipulation of cells with single-beam acoustical tweezers," *Nat. Commun.*, Vol. 11, No. 1, 4244, 2020.

46. Fu, Y. Y., C. Shen, X. H. Zhu, J. F. Li, Y. W. Liu, S. A. Cummer, and Y. D. Xu, "Sound vortex diffraction via topological charge in phase gradient metagratings," *Sci. Adv.*, Vol. 6, No. 40, eaba9876, 2020.
47. Fu, Y. Y., Y. Tian, X. Li, S. L. Yang, Y. W. Liu, Y. D. Xu, and M. H. Lu, "Asymmetric generation of acoustic vortex using dual-layer metasurfaces," *Phys. Rev. Lett.*, Vol. 128, No. 1, 104501, 2022.
48. Qian, J., Y. Wang, J. P. Xia, Y. Ge, S. Q. Yuan, H. X. Sun, and X. J. Liu, "Broadband integrative acoustic asymmetric focusing lens based on mode-conversion meta-atoms," *Appl. Phys. Lett.*, Vol. 116, No. 22, 223505, 2020.
49. Wang, Y., J. Qian, J. P. Xia, Y. Ge, S. Q. Yuan, H. X. Sun, and X. J. Liu, "Acoustic bessel vortex beam by quasi-three-dimensional reflected metasurfaces," *Micromachines*, Vol. 12, No. 11, 1388, 2021.